

## RESEARCH ARTICLE

## GAS GIANT PLANETS

# Jupiter's interior and deep atmosphere: The initial pole-to-pole passes with the Juno spacecraft

S. J. Bolton,<sup>1\*</sup> A. Adriani,<sup>2</sup> V. Adumitroaie,<sup>3</sup> M. Allison,<sup>4</sup> J. Anderson,<sup>1</sup> S. Atreya,<sup>5</sup> J. Bloxham,<sup>6</sup> S. Brown,<sup>3</sup> J. E. P. Connerney,<sup>7,8</sup> E. DeJong,<sup>3</sup> W. Folkner,<sup>3</sup> D. Gautier,<sup>9</sup> D. Grassi,<sup>2</sup> S. Gulikis,<sup>3</sup> T. Guillot,<sup>10</sup> C. Hansen,<sup>11</sup> W. B. Hubbard,<sup>12</sup> L. Iess,<sup>13</sup> A. Ingersoll,<sup>14</sup> M. Janssen,<sup>3</sup> J. Jorgensen,<sup>15</sup> Y. Kaspi,<sup>16</sup> S. M. Levin,<sup>3</sup> C. Li,<sup>14</sup> J. Lunine,<sup>17</sup> Y. Miguel,<sup>10</sup> A. Mura,<sup>2</sup> G. Orton,<sup>3</sup> T. Owen,<sup>18</sup> M. Ravine,<sup>19</sup> E. Smith,<sup>3</sup> P. Steffes,<sup>20</sup> E. Stone,<sup>14</sup> D. Stevenson,<sup>14</sup> R. Thorne,<sup>21</sup> J. Waite,<sup>1</sup> D. Durante,<sup>13</sup> R. W. Ebert,<sup>1</sup> T. K. Greathouse,<sup>1</sup> V. Hue,<sup>1</sup> M. Parisi,<sup>3</sup> J. Szalay,<sup>1</sup> R. Wilson<sup>22</sup>

On 27 August 2016, the Juno spacecraft acquired science observations of Jupiter, passing within 3000 kilometers of the equatorial cloud tops. Images of Jupiter's poles show a chaotic scene, unlike Saturn's poles. Microwave sounding reveals weather features at pressures deeper than 100 bars, dominated by an ammonia-rich, narrow low-latitude plume resembling a deeper, wider version of Earth's Hadley cell. Near-infrared mapping reveals the relative humidity within prominent downwelling regions. Juno's measured gravity field differs significantly from the last available estimate and is one order of magnitude more precise. This has implications for the distribution of heavy elements in the interior, including the existence and mass of Jupiter's core. The observed magnetic field exhibits smaller spatial variations than expected, indicative of a rich harmonic content.

The primary science goal of Juno is to improve our understanding of the origin and evolution of Jupiter, the history of the solar system, and planetary system formation in general. To constrain Jupiter's interior structure, Juno's onboard instruments probe below the cloud decks, gathering data about the planet's gravity, magnetic fields, and deep atmospheric composition. Juno's elliptical orbit provides multiple periapsis passes very close to Jupiter, within 1.06 Jupiter radii ( $R_J$ ) of the jovigraphic equator, on its pole-to-pole trajectory. Measurements associated with a second science goal use Juno's unprecedented close-in polar orbits to explore Jupiter's polar magnetosphere and intense aurorae (1).

Juno's suite of science instruments includes X-band and Ka-band communications subsystems for determining Jupiter's gravity field, dual magnetometers to map Jupiter's high-order internal magnetic field, a six-channel microwave radiometer (MWR) operating at wavelengths between 1 and 50 cm to probe Jupiter's deep atmosphere, and a color camera (JunoCam) and an infrared

spectrometer and imager (JIRAM) to capture views of Jupiter. Juno also carries a suite of field and particle instruments for in situ sampling of Jupiter's magnetosphere and investigation of its powerful aurora (2).

## The poles of Jupiter

The JunoCam instrument is a visible-light camera with blue, green, red, and methane (centered at 890 nm) filters (2). Figure 1 shows close-up three-color images of the north and south poles of Jupiter obtained 27 August 2016, resolving details as small as 50 km. The wealth of detail in these images surpasses that of previous spacecraft because their trajectories were close to Jupiter's equatorial plane, whereas Juno's orbits were closer to the planet and oriented over the poles. Only Pioneer 11 had acquired non-oblique images over Jupiter's north pole, but at 10 times the distance of Juno (3).

Within 30° planetocentric latitude from each pole, the predominant zonal banded structure of lower latitudes breaks down. This boundary is coincident with a local drop in the zonal winds

(4, 5). Within these polar regions, the banded structure is replaced by discrete features that are embedded in a background that is darker than anything at lower latitudes. The brightest features are ovals with external spiral-like extensions. A time-lapse sequence of the images reveals that the ovals are cyclones; they exhibit counterclockwise motion in the northern hemisphere. On this initial perijove pass, northern ovals cover a range of diameters from ~1400 km down to JunoCam's 50-km resolution limit. In the south, they range from 200 to 1000 km, and most lie between 71° and 74°S (all latitudes are planetocentric). In both hemispheres, some cyclones appear clustered near the poles. The other bright regions in both hemispheres are amorphous; they resemble much smaller chaotic features at lower latitudes first detected in Voyager images (6). In the north, the largest of these is on the order of 4000 to 7000 km in size. In the south, several are concentrated between 68° and 73°S and stretch over 25° of longitude (10,000 km).

Jupiter's poles appear to be different from Saturn's in two specific ways. First, there is no equivalent to Saturn's north polar hexagon (7), although circumpolar waves are observed (8). Second is the lack of a vortex that is fast ( $150 \text{ m s}^{-1}$ ), compact (2° or 2500 km in radius), and centered on the pole, like those at the north or south poles of Saturn (9, 10). Although the area within about 3° of latitude around the north pole is unilluminated, the south pole is visible and the features visible there are similar to others in the region. Thus, the polar dynamics and structures of the atmospheres of these two planets are fundamentally different. Future observations will better establish the full morphology of the poles at all longitudes and characterize their evolution in time.

An unusual high-altitude cloud is visible past Jupiter's terminator near the top portion of the north polar image in Fig. 1. It is a roughly circular feature with a diameter on the order of 7000 km. The effect of shadowing in Jupiter's clouds is evident. This cloud feature must be several scale heights ( $57 \pm 21 \text{ km}$ ) above Jupiter's main polar cloud deck to be illuminated on the nightside this far beyond the terminator. Juno cannot determine whether this is detached high-altitude haze or a towering cloud column whose base is shadowed.

## The deep atmosphere

The MWR measures thermal emission upwelling from previously unexplored depths in Jupiter's atmosphere (11, 12). Its two main scientific objectives are to determine the global abundance of ammonia and water and to observe dynamical features in the deep atmosphere. Most of our

<sup>1</sup>Southwest Research Institute, San Antonio, TX 78238, USA. <sup>2</sup>Institute for Space Astrophysics and Planetology, National Institute for Astrophysics, 00133 Rome, Italy. <sup>3</sup>Jet Propulsion Laboratory, Pasadena, CA 91109, USA. <sup>4</sup>Goddard Institute for Space Studies, New York, NY 10025, USA. <sup>5</sup>University of Michigan, Ann Arbor, MI 48109, USA. <sup>6</sup>Harvard University, Cambridge, MA 02138, USA. <sup>7</sup>Space Research Corporation, Annapolis, MD 21403, USA. <sup>8</sup>NASA Goddard Space Flight Center, Greenbelt, MD 20771, USA. <sup>9</sup>Laboratoire d'Études Spatiales et d'Instrumentation en Astrophysique, Observatoire de Paris, 92195 Meudon, France. <sup>10</sup>Université Côte d'Azur, Observatoire de la Côte d'Azur, Laboratoire Lagrange CNRS, 06304 Nice, France. <sup>11</sup>Planetary Science Institute, Tucson, AZ 85719, USA. <sup>12</sup>Lunar and Planetary Laboratory, University of Arizona, Tucson, AZ 85721, USA. <sup>13</sup>Sapienza University of Rome, 00185 Rome, Italy. <sup>14</sup>California Institute of Technology, Pasadena, CA 91125, USA. <sup>15</sup>National Space Institute, Technical University of Denmark, 2800 Kongens Lyngby, Denmark. <sup>16</sup>Department of Earth and Planetary Sciences, Weizmann Institute of Science, Rehovot 76100, Israel. <sup>17</sup>Cornell University, Ithaca, NY 14853, USA. <sup>18</sup>Institute for Astronomy, University of Hawaii at Manoa, Honolulu, HI 96822, USA. <sup>19</sup>Malin Space Science Systems, San Diego, CA 92121, USA. <sup>20</sup>Center for Space Technology and Research, Georgia Institute of Technology, Atlanta, GA 30332, USA. <sup>21</sup>Department of Atmospheric and Oceanic Sciences, University of California, Los Angeles, CA 90095, USA. <sup>22</sup>Laboratory for Atmospheric and Space Physics, University of Colorado, Boulder, CO 80303, USA.

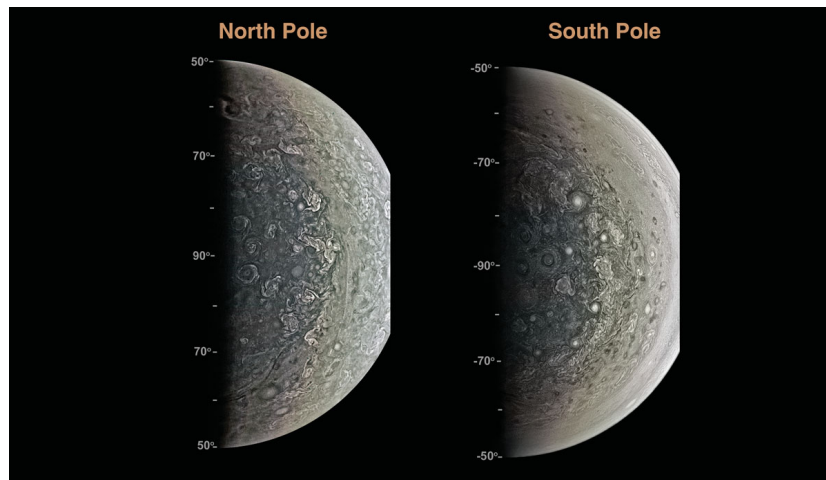
\*Corresponding author. Email: sbolton@swri.edu

current knowledge of temperatures, winds, composition, and cloud properties is confined to the tops of the clouds (i.e., to pressures of 0.5 bar or less). The Galileo probe measured atmospheric properties down to the 22-bar level at one point on the planet, and therefore did not provide a global view (13, 14). In contrast, the MWR comprises six radiometric channels operating at wavelengths from 1.4 to 50 cm that collectively sample the thermal emission from pole to pole with better than 1° resolution in latitude at the equator, and from the cloud tops to pressures as deep as several hundred bars.

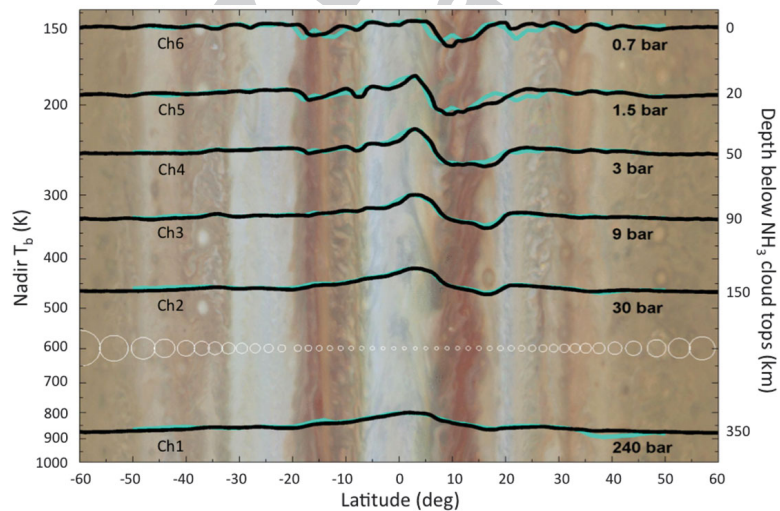
During a perijove pass, the MWR antennas scan north to south along the subspacecraft track as the spacecraft spins at 2 rpm along its orbit, obtaining overlapping measurements of the thermal radiances of each point along the track at 100-ms intervals. The radiances are converted by Planck's law to a blackbody temperature and are accordingly given in units of kelvin (15). Further, the measurements have been corrected for finite beam effects to obtain a source brightness temperature, or the effective mean radiance of Jupiter in the beam at the boresight axis, for each observation. The absolute accuracy of each measurement is 2% (uncorrelated among channels), whereas the relative accuracy (variation with respect to latitude and emission angle) at each wavelength is 0.1% (16).

Figure 2 shows plots of Jupiter's nadir brightness temperatures for all six channels, obtained during Juno's first two observational passes of Jupiter on 27 August 2016 [perijove 1 (PJ1)] and 11 December 2016 (PJ3). Only the nadir brightness is shown and used in our analysis, although the dependence of brightness on emission angle has been used to identify and eliminate data with suspected systematic errors. The brightness at each wavelength depends on the mean temperature of the atmosphere responsible for the emission, which in turn depends on the vertical distribution of opacity. The mean pressure sampled at each wavelength is indicated in the figure. Details of the radiative transfer calculations and the identification of systematic errors are given in the supplementary materials. Brightness structure with latitude is observed at all wavelengths down to ~300 bars but is seen predominantly within 20° of the equator. Comparison of PJ1 and PJ3 brightness indicates that longitudinal variations are further confined to a "weather layer" at pressures less than ~9 bars. Strong correlations among wavelengths are observed in both passes near the region of the Equatorial Zone ( $\pm 5^\circ$  latitude) and North Equatorial Belt (NEB,  $5^\circ$  to  $20^\circ$ N) at all wavelengths. The repeatability of measured brightness at high latitudes and pressure depths greater than 10 bars demonstrates both that the atmosphere is stable in these regions and that the measurements are repeatable to at least the 1% level, or approximately the widths of the lines plotted in Fig. 2 (the small dip in the Ch 1 data for PJ3 at  $40^\circ$ N is due to contamination by synchrotron emission).

We argue that the ~50 K variations of brightness temperature shown in Fig. 2 are due to var-



**Fig. 1. Orthographic projection of JunoCam color composite images of the north and south polar regions of Jupiter obtained 27 August 2016.** The north polar image was taken at 11:59 UT when the spacecraft was 73,009 km from Jupiter's cloud deck; the south polar image was taken at 13:56 UT when the spacecraft was 95,096 km from the cloud deck.



**Fig. 2. Nadir brightness temperatures in the six channels of the MWR versus planetocentric latitude.** The black and green curves are from the perijove passes on 27 August 2016 and 11 December 2016, for which the closest approaches were at 13:44 UTC and 17:05 UTC, respectively. The corresponding longitudes at equator crossing were  $97^\circ$ W and  $7^\circ$ W (system III). The frequencies of channels 1 to 6 are 0.6, 1.2, 2.6, 5.2, 10, and 22 GHz, respectively. Brightness temperature in kelvin is given at the left. Estimates of the pressure where the physical temperature is equal to the average brightness temperature are given below each curve. Underlying the plots of brightness temperature is a section of a Jupiter map taken by HST on 10 February 2016, in the visible wavelength range (PIA19643). The latitude of the bands has not changed during the months between the two data sets, but the longitudes of individual features have changed beyond the limits of the image. The white circles indicate the footprint sizes for channels 3 to 6, for which the full width at half power is  $12^\circ$  (these are shown sparsely for illustration, but the observations are in fact continuous in latitude). Channels 1 and 2 have full width at half power of  $20^\circ$ . The footprint size reflects the changing altitude of the spacecraft during its ~1-hour pass above the planet from north to south.

iations of microwave opacity. As shown in the supplementary materials, if they were due to variations of physical temperature, the wind velocities at the equator would be greater than those observed by two orders of magnitude (17). Ammo-

nia is by far the dominant source of microwave opacity in Jupiter's molecular atmosphere, surpassing that of water vapor by more than an order of magnitude and all other sources by much more (18). Therefore, we solve for the ammonia

distribution that best matches the observed brightness measurements from PJ1. In doing so, we assume that the temperature profile follows a moist adiabatic lapse rate within the clouds and transitions to a dry adiabat below at a pressure that depends on atmospheric composition (19). The results are shown in Fig. 3.

The features seen in Fig. 3 are both striking and unexpected. The dominant equatorial plume and the desiccated gas in the neighboring NEB down at least to the 60-bar pressure level resemble a giant Hadley cell. However, the ammonia crystals that fall out of the clouds evaporate before they reach the 1.5-bar pressure level. The structure is a Hadley cell without rain (17). Traditionally, but on the basis of marginal direct evidence, the ammonia has been assumed to be uniformly mixed below the clouds, with perhaps a transition region from a few bars up to its saturation level of 0.7 bar (20). The present results indicate that this is not the case, with the region of uniformly mixed ammonia confined to the region below 60 bars where it asymptotically approaches a level of 350 parts per million by volume (ppmv). We have examined modeling and experimental errors that affect our estimate, including 2% absolute uncertainties in measured brightnesses, H<sub>2</sub>O concentration varying by a factor of 10 relative to solar abundance, variations in the adiabat, uncertainties in NH<sub>3</sub> opacity, and uncorrected sidelobe contributions. We arrive at a net uncertainty in the derived ammonia concentration of ±30 ppmv, whereas the depicted ammonia concentration is seen to vary by a factor of 2 (e.g., from 350 ppmv down to 175 ppmv).

Possible causes for this structure and its implications for the general circulation of Jupiter's deep atmosphere are considered by Ingersoll *et al.* (17).

### Hot spots

The Jovian Infrared Auroral Mapper (JIRAM) provides infrared images and spectra of Jupiter's thermal emission (21). Using its dedicated imager channel on the M band (4.5 to 5.0 μm), JIRAM mapped Jupiter's upper troposphere. The coverage is almost complete between 75°N and 75°S latitude. The map in Fig. 4 was obtained by superimposing about 1000 images with variable resolution (down to a few tens of kilometers) taken during more than 1 day of observations. The mapping does not take into account the wind motion of the features, as adjacent zones are mapped one after the other, usually 30 s apart.

JIRAM geometric data are given in system III coordinates (22). The brighter regions in Fig. 4 represent areas on Jupiter where thermal radiation escapes from pressure depths deeper than a few bars. These atmospheric emissions are mostly determined by reduced opacity of the widely spread clouds. Such a low opacity allows us to probe the composition of the troposphere below the reference level of 1 bar. Those "hot spots" are thought to be areas of downwelling and hence dry air. Many hot spots occur in a zone between 5° and 20°N, within the NEB, but "excess" thermal radiation is seen from much of the planet (23, 24).

Mapping the water content inside hot spots to an unprecedented spatial resolution provides information on the cycles of condensable species and cloud formation mechanisms. The hot spot

where the water relative humidity has been retrieved and reported can be seen in Fig. 4 at about 7°N latitude, 130° longitude. The retrieval code based on the preliminary results (23) has been developed and allows reconstruction of the humidity. Results indicate a strong latitudinal dependence in the humidity distribution, a pattern that is recurrent in almost all hot spots investigated and suggests that inside the hot spot the relative humidity is lower than 3%. Results on the distribution of water and ammonia confirm a downwelling of the air in the center of the hot spot and upwelling at its edges. Values of water vapor relative humidity retrieved from the analysis of JIRAM data are typically between 5 and 8 times the values previously reported (25) for the brightest parts of hot spots. However, these values remain rather small (below 10% in the entire area around the hot spot), therefore confirming the view of these structures as dry regions in the Jupiter atmosphere. Notably, analysis of two different hot spots from JIRAM data (24) clearly shows variable contents of water vapor between different hot spots. Consequently, although differences between our results and those reported in (25) may be partially due to different retrieval methods (including adopted databases or the inclusion of a deep liquid water cloud), both analyses agree that hot spots vary over a wide range of relative humidity.

### Gravity field

The Jupiter gravity field was estimated from its effect on the Juno trajectory by measuring the Doppler shift of Juno's radio signal acquired by the NASA Deep Space Network. Juno's polar orbit and extremely low perijove make it much more sensitive to Jupiter's gravity field than those of previous missions.

For the initial science perijove (PJ1), the tracking station transmitted a signal at X-band (8 GHz). The spacecraft transponder coherently locked to this signal and transmitted signals back at X-band and Ka-band (32 GHz). With a low level of solar activity at that time, the dual-frequency downlink could be used to calibrate for the effects of charged particles in the Io plasma torus. We also used data from PJ2 on 19 October 2016 when only X-band Doppler data were available.

The data were used to estimate the gravity field parameterized by zonal harmonics through degree 12 plus sectoral and tesseral harmonics of degree 2, along with corrections to the Jupiter spin axis direction. The Juno data have less sensitivity to the Jupiter mass parameter (GM) than the data from the Galileo orbiter flybys of the Galilean satellites. We have applied a constraint to the Jupiter GM based on those data (26).

The estimated gravity harmonics are given in table S3. The odd zonal parameters for degree greater than 3 along with XXXXXX XXXXXX J<sub>10</sub> and J<sub>12</sub> are not included in table S3 because the estimated values are well below the uncertainties. The uncertainties account for both the effect of the observed data noise and from possible systematic errors. Our uncertainties include the effect of a possible gravity field of degree and order

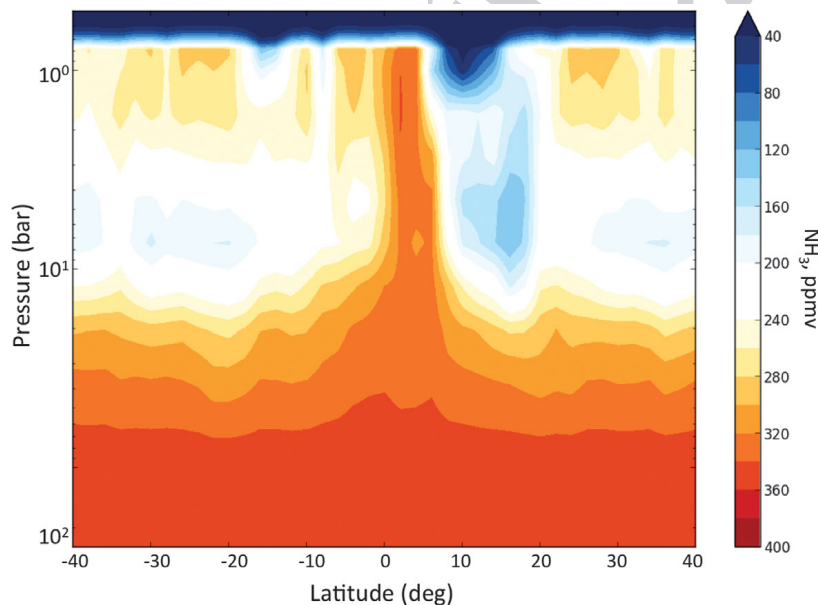


**Fig. 3. Planetocentric latitude-altitude cross section of ammonia mixing ratio.** The thin blue band at the top—near the 1-bar level—is where ammonia is condensing and the mixing ratio is low (<100 ppmv). The high mixing ratio at the equator is interpreted as air that is exchanging with the deep atmosphere at pressures of 100 bars or more, where the mixing ratio is 330 to 370 ppmv.

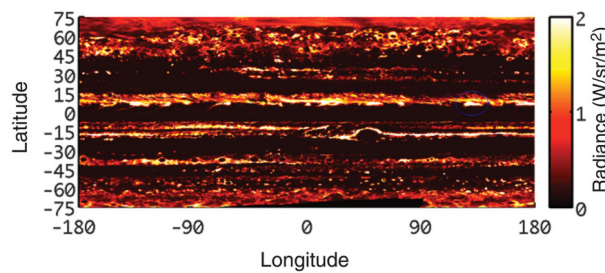
30, due to surface winds with depth of 10,000 km, that is not well sampled by data from two Juno orbits (27). (See the supplement for more details on the data noise and model used.)

Table S3 also includes earlier gravity field estimates from Pioneer and Voyager (28) and from a combination of the Pioneer and Voyager data with data from the Galileo mission (29) and with data from the Cassini and New Horizons missions (30). These are associated with ephemerides for the jovian satellites designated Jup230 and Jup310. Unlike the Juno results presented here and the earlier Pioneer and Voyager analyses, the uncertainties for Jup230 and Jup310 do not account for possible systematic errors. The uncertainties for the Juno data ignoring systematic errors are about one order of magnitude smaller than the uncertainties given here. Aside from the differences in development of uncertainties, the estimated coefficients are generally in agreement within uncertainties. The uncertainties in  $J_4$  and  $J_6$ , key parameters for constraining jovian interior models, are improved with the Juno data over earlier estimates by factors of 5 and 22, respectively. The estimated values of  $J_4$  and  $J_6$  from the Jup310 solution are significantly different from the other solutions. This is thought to be due to systematic errors in photographic observations of Amalthea by Cassini and New Horizons.

Current published interior models do not agree precisely with the Juno data, although Nettelmann *et al.*'s model (31) is close because they were fitting JUP230 harmonics, a previous determination by Jacobson (29) that is also close to the Juno results. Figure 5 shows that recent models, all of which have  $J_2$  consistent within the uncertainty of the Juno determination, show a significant scatter in  $J_4$  and, to a lesser extent, in  $J_6$ . At the level of accuracy provided by the Juno measurements, differential rotation can affect these harmonics. We expect to get a better understanding of differential rotation by looking at small higher harmonics (e.g.,  $J_8$ ,  $J_{10}$ ) and the odd harmonics that do not exist in hydrostatic equilibrium (e.g.,  $J_3$ ). The models have varying interior temperatures, heavy element distributions, and core masses. Some of the differences in predicted gravity arise from uncertainties in the equation of state for hydrogen-helium mixtures, the assumption of an adiabatic interior and the effects of helium immiscibility. Wahl *et al.* (32) presented a possible interpretation for the Juno data that requires a core that is dispersed out to perhaps as much as  $0.5R_J$ . An assessment of this and other possibilities must await additional Juno observations. The addition of heavy elements, in particular water, is important and we expect to place constraints on this from the microwave observations. Magnetic field data may also reduce the ambiguity of interpretation.

**Magnetic field**

The Juno spacecraft ventured closer to Jupiter's surface than previous spacecraft, passing to within  $1.06 R_J$  of its center on its pole-to-pole trajectory. Juno's magnetometer (33) sampled at a rate of 64 vector samples/s throughout its closest ap-



**Fig. 4. Cylindrical map of the infrared emission from Jupiter as detected by JIRAM.** The map is colored according to radiance in  $W m^{-2} sr^{-1}$  integrated from 4.5 to  $5.0 \mu m$ . System III reference frame is used.

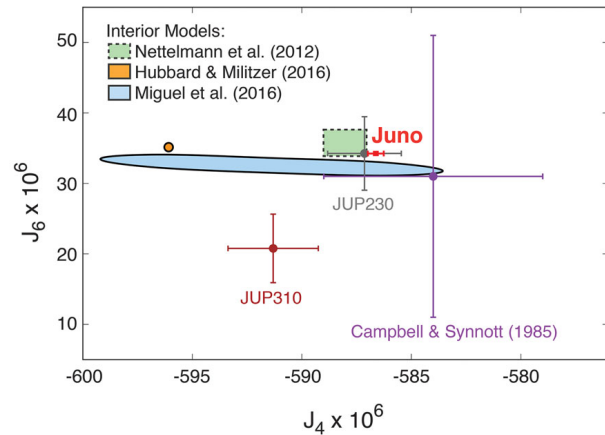


**Fig. 5. Jupiter gravitational field coefficients  $J_4$  and  $J_6$ .** Pre-Juno observations from Campbell and Synnott (1985) (28) (purple), Jacobson (2003) (29) (JUP230, gray), and Jacobson (2013) (30) (JUP310, brown) are compared to Juno's preliminary measurement (red); values are given in table S3. Overlain are model predictions by Nettelmann *et al.* (2012) (31), Hubbard and Militzer (2016) (40), and Miguel *et al.* (2016) (41).

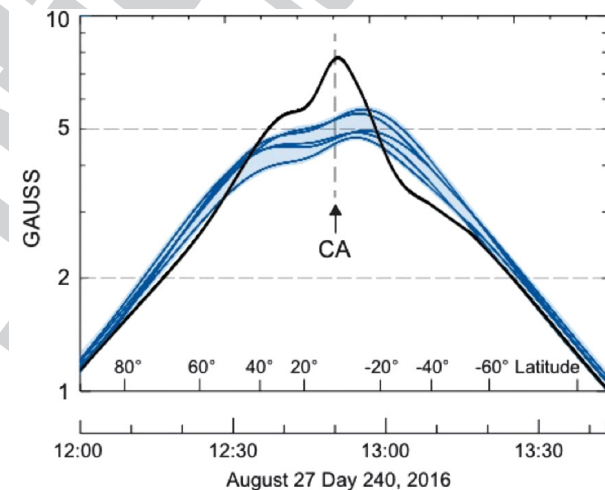


**Fig. 6. Magnitude of the magnetic field observed along Juno's closest approach trajectory (solid line) as a function of time and spacecraft latitude, compared with that computed from a suite of existing models (35).** The stippled region illustrates the range of such model predictions, bounded by the VIP4 model beneath and the GSFC O4 model above.

proach, recording a magnetic field that greatly exceeded expectations based on existing models (Fig. 6). The maximum magnetic field observed during this periapsis was 7.766 G, more than an order of magnitude greater than Earth's maximum (south polar) surface field magnitude (0.66 G). The observed magnetic field displays more spatial variation relative to that represented by low degree and order spherical harmonic models, in-

dicative of a rich harmonic content awaiting Juno's mapping phase. Juno's mapping phase is designed to envelop Jupiter in a dense net of observations equally distributed in longitude, and this initial pass indicates that the mapping phase will reveal a field rich in higher harmonics.

Although many spacecraft have sampled Jupiter's powerful magnetic field, none have sampled the field well inside of Io's orbit ( $5.95R_J$ ) since the

F5

F6

flybys of Pioneer 10 and Pioneer 11 during the early 1970s. Our knowledge of Jupiter's magnetic field is thus limited by a paucity of direct observation close to the planet's surface, reflected in spherical harmonic models (34, 35) that are confined to low degree and order, typically 3 or 4. The model field in widespread use and adopted by the Juno Project uses observations of the Io flux tube footprint as an additional constraint, but even so, this model's degree and order 4 terms are only partially resolved. Figure 6 compares the observed field magnitude with that calculated from a suite of such models (35), demonstrating that none adequately characterize the field near the surface.

Characterization of the field to high degree and order allows one to estimate the depth to the dynamo region, under the assumption that the harmonic spectrum is essentially "white" at the core surface—that is, represented by harmonic terms of equal amplitude by degree. Earth's dynamo radius ( $\sim 0.5R_E$ ) may be located in this way and is consistent with seismic observations of the fluid core. The dynamo surface may also be located using the frozen flux theorem if variation of the magnetic field with time can be detected. The rich harmonic content indicated by Juno's initial (instrumented) periapsis pass portends a dynamo generation region not far beneath the surface. This may indicate that dynamo generation in Jupiter's interior—a process that requires electrically conducting fluid in convective motion—may occur in the molecular hydrogen layer above the pressure-induced transition to the metallic state, as first suggested by Smoluchowski (36). Experimental data (37) indicate significant electrical conductivity in dense molecular hydrogen. Theoretical estimates consistent with these data (38) allow for a conductivity  $\sigma \sim 1.5 \times 10^5$  S/m at  $0.89R_J$  and  $\sigma \sim 1.5 \times 10^3$  S/m at  $0.93R_J$ . These values suggest a magnetic Reynolds number of  $Re_m \equiv \mu_0 \sigma v L \sim 10^3$  to 10 for these radii, assuming a characteristic fluid velocity  $v \sim 0.01$  m/s and characteristic length scale  $L \sim 1000$  km, both plausible choices for dynamo generation in Jupiter (39).

### Summary

The results from Juno's initial close passes of Jupiter are changing our understanding of this gas giant. Juno's direct glimpse of Jupiter's poles shows numerous cyclonic storms clustered together

and a storm illuminated in Jupiter's nightside that provided a measurement of its vertical extent. The deep microwave sounding of Jupiter by Juno demonstrates the power of this technique for unveiling spatial and temporal structure in the ammonia abundance. The initial measurement of Jupiter's gravity will inform interior models with implications for the extent, existence, and mass of Jupiter's core. The magnitude of the observed magnetic field observed was 7.766 G, almost twice as strong as expected. More results from Juno's initial passes are discussed in a companion paper (I).

### REFERENCES AND NOTES

- J. E. P. Connerney et al., *Science* **356**, XXXX (2017).
- C. J. Hansen et al., *Space Sci. Rev.* 10.1007/s11214-014-0079-x (2014).
- T. Gehrels, in *Jupiter: Studies of the Interior, Atmosphere, Magnetosphere and Satellites*, T. Gehrels, Ed. (Univ. of Arizona Press, 1976), pp. 531–563.
- E. García-Melendo, A. Sánchez-Lavega, *Icarus* **152**, 316–330 (2001).
- X. S. Asay-Davis, P. S. Marcus, M. H. Wong, I. de Pater, *Icarus* **211**, 1215–1232 (2011).
- A. P. Ingersoll et al., *Nature* **280**, 773–775 (1979).
- D. A. Godfrey, *Icarus* **76**, 335–356 (1988).
- N. Barrado-Izaguirre, S. Perez-Hoyos, A. Sánchez-Lavega, *Icarus* **202**, 181–196 (2009).
- A. Antuñaño, T. del Río-Gaztelurrutia, A. Sánchez-Lavega, R. Hueso, *J. Geophys. Res.* **120**, 155–176 (2015).
- U. A. Dyudina et al., *Icarus* **202**, 240–248 (2009).
- M. A. Janssen et al., *Icarus* **173**, 447–453 (2005).
- M. A. Janssen et al., *Space Sci. Rev.* 10.1007/s11214-017-0349-5 (2017).
- W. M. Folkner, R. Woo, S. Nandi, *J. Geophys. Res.* **103**, 22847–22855 (1998).
- M. H. Wong, P. R. Mahaffy, S. K. Atreya, H. B. Niemann, T. C. Owen, *Icarus* **171**, 153–170 (2004).
- M. A. Janssen, Ed., *Atmospheric Remote Sensing by Microwave Radiometry* (Wiley, 1993).
- S. T. Brown, M. A. Janssen, S. Misra, *Geophys. Res. Lett.* (2017).
- A. P. Ingersoll, C. Li, M. A. Janssen, *Geophys. Res. Lett.* (2017).
- P. G. Steffes et al., *Space Sci. Rev.* **XXX**, XXXX (2017).
- C. Li, A. P. Ingersoll, F. Oyafuso, S. Ewald, M. A. Janssen, *Geophys. Res. Lett.* (2017).
- S. K. Atreya, A. S. Wong, K. H. Baines, M. H. Wong, T. C. Owen, *Planet. Space Sci.* **53**, 498–507 (2005).
- A. Adriani et al., *Space Sci. Rev.* 10.1007/s11214-014-0094-y (2014).
- B. A. Archinal et al., *Celestial Mech. Dyn. Astron.* **109**, 101–135 (2010).
- G. Sindoni et al., *Geophys. Res. Lett.* **XXX**, XXXX (2017).
- D. Grassi et al., *Geophys. Res. Lett.* **XXX**, XXXX (2017).
- M. Roos-Serote, S. K. Atreya, M. K. Wong, P. Drossart, *Planet. Space Sci.* **52**, 397–414 (2004).
- R. Jacobson, R. Haw, T. McElrath, P. Antreasian, *Adv. Astronaut. Sci.* **103**, 465–486 (1999).
- M. Parisi, E. Galanti, S. Finocchiaro, L. Less, Y. Kaspi, *Icarus* **267**, 232–242 (2016).
- J. K. Campbell, S. P. Synnott, *Astrophys. J.* **90**, 364–372 (1985).
- The JUP230 solution corresponds to the gravity field of Jupiter calculated by R. A. Jacobson in 2003 using Pioneer, Voyager, and Galileo data as released on [http://ssd.jpl.nasa.gov/?gravity\\_fields\\_op](http://ssd.jpl.nasa.gov/?gravity_fields_op)
- The JUP310 solution corresponds to the gravity field of Jupiter calculated by R. A. Jacobson in 2013 using Pioneer, Voyager, Galileo, and New Horizons data as released on [http://ssd.jpl.nasa.gov/?gravity\\_fields\\_op](http://ssd.jpl.nasa.gov/?gravity_fields_op)
- N. Nettelmann, A. Becker, B. Holst, R. Redmer, *Astrophys. J.* **750**, 52 (2012).
- S. Wahl et al., *Geophys. Res. Lett.* **XXX**, XXXX (2017).
- J. E. P. Connerney et al., *Space Sci. Rev.* 10.1007/s11214-017-0334-z (2017).
- J. E. P. Connerney, M. H. Acuña, N. F. Ness, T. Satoh, *J. Geophys. Res.* **103**, 11929–11939 (1998).
- J. E. P. Connerney, Planetary magnetism. In G. Schubert, T. Spohn, Eds., *Treatise on Geophysics, Volume 10: Planets and Satellites* (Elsevier, 2015), pp. 195–237; <https://ntrs.nasa.gov/archive/nasa/casi.ntrs.nasa.gov/20150011017.pdf>.
- R. Smoluchowski, *Astrophys. J.* **200**, L119–L121 (1975).
- W. J. Nellis, S. T. Weir, A. C. Mitchell, *Science* **273**, 936–938 (1996).
- M. French et al., *Astrophys. J. Suppl. Ser.* **202**, 5 (2012).
- T. Guillot, D. J. Stevenson, W. B. Hubbard, D. Saumon, in *Jupiter*, F. Bagenal, T. Dowling, W. B. McKinnon, Eds. (Cambridge Univ. Press, 2004), chap. 3.
- W. B. Hubbard, B. Militzer, A preliminary Jupiter model. *Astrophys. J.* **820**, 80 (2016).
- Y. Miguel, T. Guillot, L. Fayon, *Astron. Astrophys.* **596**, A114 (2016).

### ACKNOWLEDGMENTS

We acknowledge the important contributions of M. H. Acuña, A. Coradini, and M. J. Klein to the Juno project. The images in Fig. 1 were processed by citizen scientist R. Tkachenko as part of Juno's outreach program. The visible map shown in Fig. 2 is based on observations made with the NASA/ESA Hubble Space Telescope (HST) under program GO14334, the Outer Planet Atmospheric Legacy Program (see [MWR-14]). Supported by the Juno project under NASA grant NNM06AA75C to Southwest Research Institute; NASA grant NNN12AA01C to the Jet Propulsion Laboratory; Centre National d'Études Spatiales (T.G. and Y.M.); and Agenzia Spaziale Italiana (ASI) (A.A., D.G., L.I., and A.M.). The JIRAM and KaT instruments are funded by ASI; HST is funded by NASA through a grant from the Space Telescope Science Institute, which is operated by the Association of Universities for Research in Astronomy Inc. under NASA contract NAS5-26555. All maps from this program can be retrieved at <https://archive.stsci.edu/prepds/opal/>. Supporting data are available in the supplementary materials. As agreed with NASA, fully calibrated Juno data are released on schedule via the NASA Planetary Data System at <https://pds.nasa.gov/>.

### SUPPLEMENTARY MATERIALS

[www.sciencemag.org/content/356/63XX/PAGE/suppl/DC1](http://www.sciencemag.org/content/356/63XX/PAGE/suppl/DC1)  
Materials and Methods  
Figs. S1 to S4  
Tables S1 to S4  
References (42–63)

13 December 2016; accepted 1 May 2017  
10.1126/science.aal2108